



Electron beam powder bed fusion manufacturing of a Ti-5Al-5Mo-5V-3Cr alloy: a microstructure and mechanical properties' correlation study

Julius Hendl^{1,2} · Axel Marquardt^{1,2} · Christoph Leyens^{1,2}

Received: 28 October 2021 / Accepted: 15 August 2022 / Published online: 7 October 2022
© The Author(s) 2022

Abstract

Electron beam powder bed fusion (EB-PBF) is a powder-bed fusion additive manufacturing process, which is suitable for fabricating high-performance parts for a wide range of industrial applications, such as medical and aerospace. Due to its deep curing capabilities, the metastable β -alloy Ti-5Al-5Mo-5V-3Cr (Ti-5553) is currently mostly used in the landing gear of airplanes. However, its great mechanical properties make it also attractive for small, complex, and load-bearing components. In this study, nine melting parameter sets, combining different scanning speeds and beam currents, were used in the EB-PBF ARCAM A2X system. Furthermore, the correlation between the microstructure and the mechanical properties was investigated and analyzed by applying μ -focus computer tomography and microscopic methods (optical, SEM/EDS). A significant influence of the different melting parameters on the microstructure as well as on the mechanical performance was found. In a subsequent step, three melting parameters were selected and the specimens were heat-treated (BASCA, STA) for further investigation. The experimental results of this work indicate that Ti-5553 parts can be manufactured successfully with high quality ($\rho > 99.60\%$), and post-processing heat-treatments can be used to modify the microstructure in such a way that the parts are suitable for a large variety of possible applications.

Keywords Additive manufacturing · Electron beam powder bed fusion · Titanium alloys · Process–structure–property relationship · Defect characteristics · Non-destructive evaluation

1 Introduction

Today's fast-moving industry is a tremendous demand for new lightweight materials and novel design capabilities. To meet this need, it is essential to use new manufacturing technologies, such as Electron Beam Powder Bed Fusion (EB-PBF). New materials are especially needed in the aerospace industry to obtain a better strength-to-weight ratio [1]. Ti-5Al-5Mo-5V-3Cr (wt.-%) (Ti-5553) with a density of 4.67 g/cm^3 [2] exhibits excellent mechanical properties, such as high strength, good ductility, and excellent fatigue characteristics. These can be varied easily through different

heat-treatment processes. Ti-5553 was developed from the Russian VT 22 (Ti-5Al-5Mo-5V-1Cr-1Fe) alloy. In the next few years, it is expected to replace the currently most used near beta titanium alloy Ti-10V-2Fe-3Al (Ti-1023), due to its enhanced mechanical performance and workability [2]. The mechanical properties of Ti-5553 are mainly dependent on the microstructure, consisting of a bcc β -matrix and hcp α precipitations. It has been shown that for Ti-5553, the coherency at the interfaces between the α and β phases is increased [3] compared to conventional α/β -alloys (e.g., Ti-6Al-4V, [4–6]). Thus, it can be expected that the activation energy needed to precipitate α is reduced, due to the reduction of misfit coherency strains at the nucleation sites along these interfaces. As a result of this reduction very fine α can be precipitated [3, 7]. The shape, size, and distribution of the α precipitations can strongly influence the mechanical properties [8]. Depending on the nucleation time, these have to be differentiated into primary (α_p , forming under isothermal heat-treatment below the T_β or during slow cooling from above the T_β) and secondary α (α_s , forming by

✉ Julius Hendl
julius.hendl@tu-dresden.de

¹ Institute of Materials Science, Technische Universität Dresden, Helmholtzstr. 7, 01069 Dresden, Germany

² Fraunhofer-Institute for Material and Beam Technology (IWS), Winterbergstraße 28, 01277 Dresden, Germany

aging at lower temperatures) precipitations [9]. By using different heat-treatments, the microstructure of Ti-5553 can be tailored. Depending on the precipitation fractions, the yield strength (YS) and the ultimate tensile strength (UTS) can be almost as large as 1300 MPa [10] and 1500 MPa [11], respectively. In comparison, the obtainable mechanical properties of the most commonly used α/β Ti-6Al4V alloy are much lower (YS of 1100 MPa and UTS of 1200 MPa) [12]. The ductility of the Ti-5553 alloy mainly depends on the combination of the size and distribution of β -grains and α_p precipitations. Decreasing the β -grain size in combination with obtaining larger α precipitations improves ductility and thus fatigue properties [12]. Due to its good deep hardening properties (up to 150 mm) and castability [13], Ti-5553 is used for large structural parts of airplane landing gear modules (e.g., parts of the Boeing Dreamliner 787) [13]. However, owing to the poor machinability of the alloy [14] as well as limitations in the freedom of the design in conventional manufacturing processes (e.g., casting, forging, and milling) [15], the manufacturing of complex parts is very challenging, if not impossible, and often not cost-efficient. To open the market for complex-shaped and load-bearing parts built out of Ti-5553, alternative manufacturing routes have to be utilized. Since the mid-1980s, additive manufacturing (AM) processes have been used to build printed components [16] by adding layers of materials to each other and creating a permanent bond between them. Thus, many previously existing design limitations can be overcome [17, 18], and using technologies like topology optimization, further significant improvements can be achieved [19]. Other advantages of AM include the ability to produce prototypes or small batches with high resource efficiency and without the need for additional tooling; thus, it becomes more costly as well as time-efficient [20–22]. EB-PBF is a modern, powder-bed fusion, AM process route with great potential. The scanning speed, as well as the energy density of an EB-PBF process, is higher than for other powder bed processes, such as Laser Powder Bed Fusion (L-PBF). This results in increased build rates when using EB-PBF compared to L-PBF. Due to its layer-by-layer process, metal components with unique geometry and microstructure can be easily manufactured. For this process, a sliced 3D-CAD model is transmitted into the machine, and the electron beam melts the powder sequentially. To direct the electron beam precisely, the process takes place under a vacuum. Another upside of the vacuum is that reactive metals such as titanium and their alloys [23] can be processed without the risk of oxygen contamination. Research has shown that under these conditions, contamination by oxygen and nitrogen is very low and has no effect on the mechanical properties [24]. One problem with the application of additively manufactured parts is the process-related defects, such as lack of fusion, gas porosity, unmelted powder, swelling, or cracks. Defects

can occur if the melting parameter is not optimized or powder is not properly distributed on the build platform [1]. Both the morphological properties (size, shape, and distribution) and the quantity of defects can influence the mechanical behavior dramatically [25, 26]. A study by Liu et al. [27] has shown that for static mechanical properties defects have only a minor to almost no impact. In comparison, defects have a great influence on fatigue properties, and these defects, especially irregularly shaped defects, act as crack nuclei and reduce life expectancy [28, 29]. Further disadvantages of the AM process, in general, are the high investment cost of machinery and the high maintenance required, the poor surface quality, and the thermally introduced stresses [20–22]. Ti-5553 has been manufactured additively with the L-PBF process as well as using direct energy deposition processes (details of these processes will not be discussed further in this work) [30, 31]. For L-PBF, the achieved relative density was measured by Zopp et al. [32] to be in the range of 97.92 to 99.97% and by Schwab et al. [33] from 99.00 to 99.50%. When working without a heated stage, the as-built microstructure using L-PBF shows a very large grain size and a pure β -microstructure [33]. When substrate heating is used an additional very fine α -phase (needles with less than 500 nm in length) can be seen [34]. L-PBF as built Ti-5553 samples with a pure β -microstructure shows an elongation at break of 14% and a UTS of 800 MPa [33]. Ti-1023 [35, 36] and Ti-1Al-8V-5Fe (Ti-185) [37] are other metastable β -titanium alloys that are currently under research and have been additively manufactured using the L-PBF process [38]. Liu and Qui show in their work [35, 36] that samples with a relative density of > 99.50% can be reached. Due to the large cooling rate during L-PBF, the obtained microstructure of the samples prepared with high- or low-laser power shows a β -matrix and a very fine athermal ω -phase, respectively. The presence of a ω -phase reduces the mechanical strength dramatically [12]. In addition, nanoscale α precipitates could be detected in the microstructure during the vertical buildup of the low-energy density samples [36]. These various microstructures lead to a range of different mechanical properties, with a UTS up to 939 MPa and an almost 14% elongation at break for samples with an α free microstructure. When α precipitation occurred, there was a significant reduction of the elongation at break to less than 2% in the test specimens [35, 36]. The microstructure of L-PBF manufactured Ti-185 always showed a β -matrix as well as α and ω precipitations [37]. During the heat treatment above 500 °C, it was found that the ω -phase often transforms into the β -phase [3].

The combination of the design freedom, the enhanced mechanical strength, and the high elongation properties of the EB-PBF manufactured Ti-5553 parts, make this alloy very interesting for small, complex, and load-bearing parts. This study shows the dependence of the density, and microstructure on different process parameter sets of EB-PBF

manufactured Ti-5553 alloy. Consequently, a stable process window for the manufacture of a Ti-5553 alloy using the EB-PBF process was found and different melting parameters (varying the line energy) were tested. Methods such as optical and selective electron microscopy, X-ray diffraction (XRD), tensile and hardness tests, and extensive μ -focus computed tomography (μ -CT) studies were used to evaluate relative density, microstructure, and mechanical properties. To tailor the mechanical properties of Ti-5553 alloy with subsequent heat treatment for the application, three suitable melting parameters were selected based on its unique microstructure, mechanical properties, and distribution and structure of defects. By varying the heat-treatment parameters, the different microstructural constituents can be adjusted selectively, and thus, tailored mechanical properties can be produced.

2 Materials and methods

2.1 Powder

The powder used for the EB-PBF process is produced by gas atomization. Due to the advantageous particle-size distribution, the Plasma Inert Gas Atomisation–PIGA method is often used to produce such powders [39]. The melted material is fed through a nozzle and diffused by a stream of argon. The process results in a highly spherical and pure powder [40] which has excellent characteristics for the EB-PBF process see Fig. 1. To ensure optimum built results (regarding density, etc.), the internal porosity of the powder should be as low as possible, as shown in Fig. 2. To reduce the sintering activity of the powder and to achieve good flowability, a coarse powder is preferred in the EB-PBF process [39].

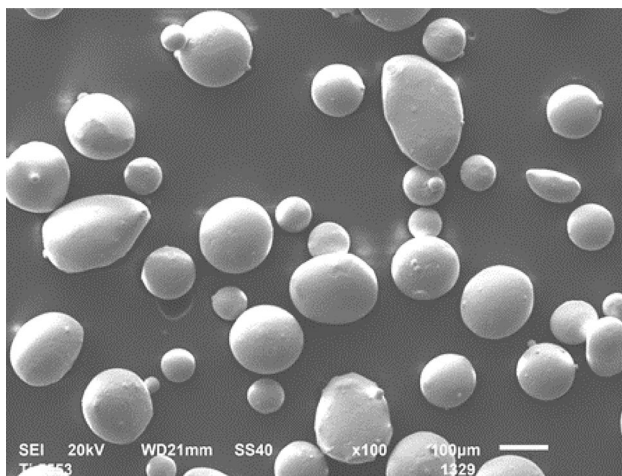


Fig. 1 Powder morphology of as-received PIGA atomized Ti-5553 powder, SEM

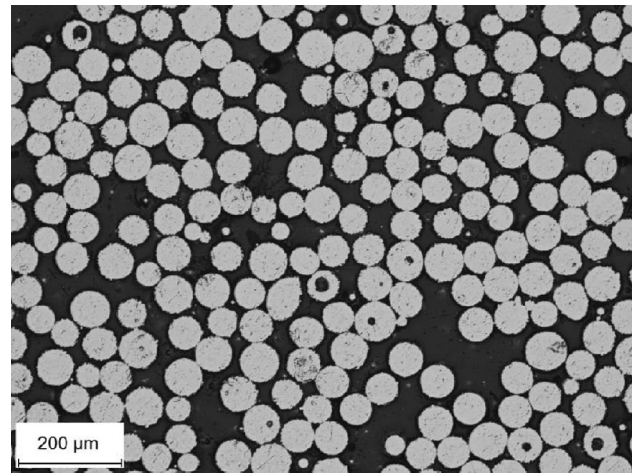


Fig. 2 Inner porosity of as-received PIGA atomized Ti-5553 powder, optical microscope

Therefore, the powder used in this study had a powder particle-size distribution from 45 to 150 μm ($d_{50} = 71.46 \mu\text{m}$, $O_2 = 900 \text{ ppm}$).

2.2 The EB-PBF process

The machine utilized in this study was an ARCAM A2X with a maximum beam power of 3000 W and a beam transition speed of up to 8000 mm/s. An EB-PBF production run always consists of the same procedure: lowering of the build platform-application of the powder–preheating–melting–reheating. After the powder has been evenly distributed onto the starting plate, a preheating step with a defocused electron beam is mandatory to slightly sinter the powder [41]. To keep the desired process temperature almost constant during the manufacturing process, intermediate reheating has to be introduced after each build cycle. Otherwise, there would be a risk that the pre-sintering of the powder particles would be insufficient, and the so-called smoke effect would occur. Investigations have shown that process-aborting smoke effects are evident at temperatures below 550 $^{\circ}\text{C}$ and swelling occurs above 720 $^{\circ}\text{C}$. Therefore, a preheating temperature of 660 $^{\circ}\text{C} \pm 12 \text{ }^{\circ}\text{C}$ was used. Figure 3 shows the temperature–time cycle of the process temperature measured under the starting plate as well as the column temperature during the production run. To ensure proper bonding between the starting plate and the powder, the powder under the start plate was lightly sintered for 20 min. As a consequence, a small temperature drop can be seen at the beginning of the process.

When working under vacuum conditions (10^{-3} – 10^{-5} mbar) and at high temperatures, alloying elements with high partial pressures are likely to evaporate [24] when melted with a focused electron beam. The specimens manufactured for this

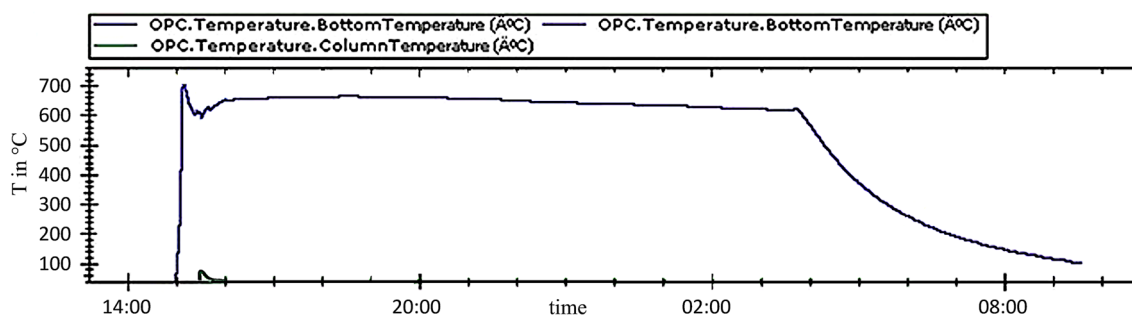


Fig. 3 Temperature–time diagram during the EB-PBF process, where the thermocouple is located under the build platform

study had a cylindrical geometry ($h = 100$ mm, $\varnothing = 10$ mm). To understand the correlation between the used melting parameters and the resulting, microstructure, porosity, and mechanical properties, different parameter combinations were investigated in this work. Thus, using a constant accelerating voltage ($U = 60$ kV) and varying the scanning speed (v_s) and/or the beam current (I_B) samples with different line energies (E_L), see Eq. (1), were manufactured. The used manufacturing parameters are shown in Table 1

$$E_L = U \times \frac{I_B}{v_s} \quad (1)$$

2.3 Analytic methods

Density analyses were performed using several methods, such as hydrostatic pressure (Archimedes principle), optical measurement, and μ -CT with an ff35 from YXLON International GmbH, which has a resolution of about $6.5 \mu\text{m}/\text{voxel}$. Optical measurements were performed with a Nikon Optiphot, where 5 images per sample were examined and porosity determined using an ImageJ[®] script. The relative density (ρ_{rel}) can be calculated, see Eq. (2), by subtracting the porosity (ρ_{porosity}) from 100%

$$\rho_{\text{rel}} = 100\% - \rho_{\text{porosity}} \quad (2)$$

The microstructure was investigated on specimens cut out of EB-PBF manufactured cylinders. To analyze the microstructure specimens underwent an additional process of grinding and polishing. The preparation route consisted of

four grinding stages (P240 to P2500) and one final polishing stage. For this latter step 100 ml oxide polishing suspension, OPS was mixed with 2 ml each of ammonia and hydrogen peroxide, and the specimens were polished for 11 min to remove the remaining Beilby layer.

To identify the phases after the EB-PBF process, the samples were analyzed by XRD, using a Bruker D8 Discover X-ray diffractometer and applying $\text{Cu-K}\alpha$ radiation. A Goebel mirror with a 0.5 mm round aperture and 0.5 mm collimator was used on the primary side. On the secondary side, a VANTEC 500 area detector was used. Measurements were carried out using coupled θ – 2θ scans. For phase identification Match! 3 from Crystal Impact GbR along with the crystallography open database (COD) was used.

To study and evaluate the achieved microstructure after each processing step, SEM pictures were recorded using a Zeiss DSM 982 Gemini. The SEM pictures were analyzed to measure the α_p fraction, by utilizing the ImageJ[®] trainable waka script. To measure the composition using energy-dispersive spectroscopy (EDS), a Thermo Scientific UltraDry mounted on a Zeiss DSM 950 was used. The electron back-scattered diffraction (EBSD) was carried out using a NordlysNano EBSD detector, mounted on a Jeol JIB-4610F (SEM), and the Aztec data acquisition software.

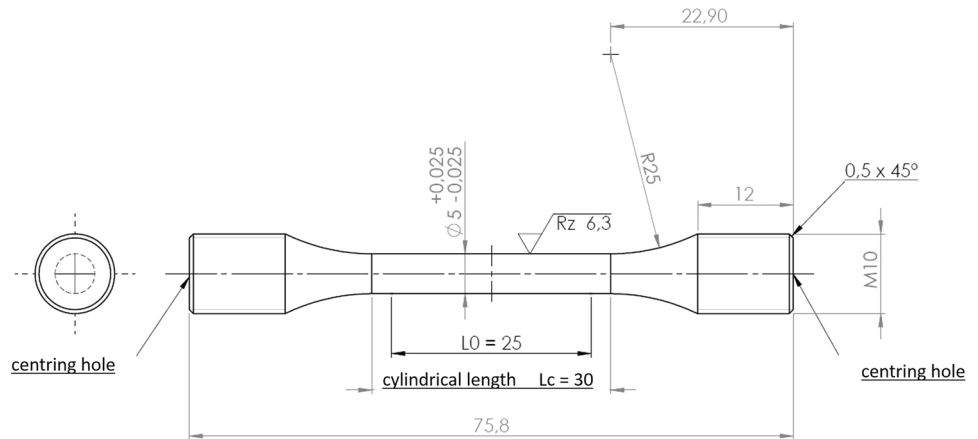
To perform the study of static mechanical properties, the cylindrical specimens were machined to the target geometry using a milling cutter, see Fig. 4. The tensile test was made on a Zwick 1474, according to DIN EN ISO 6892-1 [42], using a steady elongation rate of 0.55 mm/min. For each parameter set, three individual specimens were tensile tested. A KB 250BVZ equipped with a Vickers tip was used

Table 1 Manufacturing parameters and used E_L (J/m) for each parameter set (P)

Beam current	5 mA	10 mA	15 mA
Scanning speed			
4000 mm/s (parameter sets 1–3, l. E_L)	75 J/m—P1	150 J/m—P2	225 J/m—P3
1500 mm/s (parameter sets 4–6, m. E_L)	200 J/m—P4	400 J/m—P5	600 J/m—P6
500 mm/s (parameter sets 7–9, h. E_L)	600 J/m—P7	1200 J/m—P8	1800 J/m—P9

l. low, *m.* medium, *h.* high

Fig. 4 Tensile test specimen geometry following DIN EN ISO 6892 [42]



to quantify the hardness (HV10) according to DIN EN ISO 6507-1 [43]. Therefore, five hardness measurements were performed and analyzed on one specimen for each tested parameter set.

2.4 Heat-treatment regime

Heat treatments for metastable β -titanium alloys often follow a similar cycle. To dissolve the as-built microstructure, usually, solution treatment is followed by quenching and subsequently an aging process. Depending on the treatment procedure (time and temperatures), different microstructures and therefore mechanical properties can be achieved. In this work, three different heat treatments were investigated. All heat-treatments were made under an argon gas flow atmosphere (Ar 5.0) to prevent any oxygen pick up of the samples. After each aging step, the samples were furnace cooled to room temperature.

The solution-treated and aged (STA) heat treatment is used for parts with high-strength requirements. Specimens are solution-treated at 790 °C for 1 h (beneath T_{β}), air quenched to room temperature, and aged at low temperatures (500 °C, 1 h). To maximize the fatigue and fracture toughness in combination with high strength [44], different approaches were investigated. Therefore, the specimens were beta annealed and slow cooled and aged (BASCA) at higher temperatures compared to the STA regime. In this work, two slightly different BASCA regimes were investigated. The BASCA I regime combines a solution treatment at 870 °C for 1 h, air quenching to room temperature, and then aging (570 °C, 8 h). In comparison, the annealing temperature and time were higher and longer for the BASCA II regime (890 °C, 1.5 h). Furthermore, the specimens were furnace cooled from the annealing temperature to the aging temperature of 600 °C at 2 K/min and were held there for 8 h.

3 Results

3.1 Density

In this study, all specimens show a relative density higher than 99.00%, varying between 99.34% and 99.89%. The analysis of the μ -CT data, see Fig. 5, shows a homogeneous distribution of defects all over the sample volume.

In Table 2, correlations between the used parameter sets and the resulting defects are summarized. Furthermore, differences between the average defect count, defect size, and the density of the specimens manufactured with different melting parameter sets are shown. When using a low E_L (75–225 J/m), the highest average density was achieved. While, a moderate E_L (400–600 J/m) leads to the lowest (average) densities.

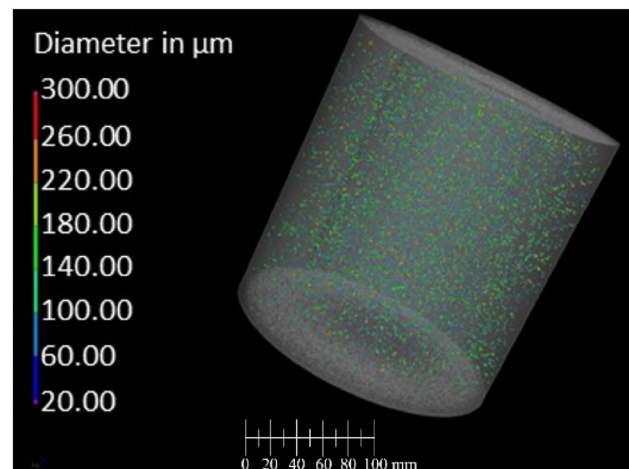


Fig. 5 3D reconstructed volume with visualized internal defects of an EB-PBF manufactured Ti-5553 alloy using an E_L of 150 J/m (P2)

3.2 As-built mechanical properties and microstructure

In Table 3, the α_p fraction of the as-built samples, and thus, the resulting mechanical properties are summarized. The samples manufactured with the lowest E_L show the highest mechanical strength but the lowest elongation at break. The use of higher E_L leads to better elongation at break (P8 shows an almost 100% higher elongation at break than P2) and slightly lower strength. The resulting graphs of the tensile tests are summarized in Fig. 9.

Two fracture surfaces of as-built specimens after tensile testing are shown in Fig. 6. The respective constrictions can be correlated with the elongations at break. Specimens that break at lower elongation (P2) cannot deform as much and therefore show less constriction as specimens with a higher elongation at break (P6).

To exclude any enrichment or depletion of alloying elements during the manufacturing process (as discussed in

Sect. 2.2), the samples were analyzed for their chemical composition using EDS measurements. Each EDS measurement showed a composition that was inside the boundaries of the ASTM standard. This proves that no aluminum evaporation has occurred during the manufacturing process.

XRD was used to identify the phases after the manufacturing process, see Fig. 7. The peaks could be assigned to the α -phase [45] and the β -phase [46]. The distribution of crystal orientation shown in Fig. 8 does not indicate a strong build related orientation. Every specimen, regardless of the used parameter set, shows the same phases that differ in their proportions: a large-grained β -titanium-matrix, large lamellar α_p , and fine, mostly acicular α_s precipitations.

3.3 Heat treatment

Heat treatments are used to influence the microstructure and thus adjust the mechanical properties. As shown in Sect. 2.3, three different heat treatments were performed

Table 2 Dependence of the average density and defect characteristics on E_L of EB-PBF manufactured Ti-5553 alloy

	Parameter sets 1–3	Parameter sets 4–6	Parameter sets 7–9
Avr. defects count	115,952 ± 4673	228,202 ± 69,259	163,744 ± 16,148
Avr. defects size in μm	94.4 ± 0.7	90.5 ± 3.4	85.9 ± 1.1
Avr. density in %	99.85 ± 0.03	99.66 ± 0.12	99.77 ± 0.04

Table 3 Dependence of the α_p fraction and resulting mechanical properties on E_L when using a constant beam current but different scanning speed during EB-PBF of a Ti-5553 alloy

	α_p in %	YS in MPa	UTS in MPa	El. at break in%	HV10
P2 (150 J/m)	28.5 ± 1.3	948 ± 19	1016 ± 4	4.9 ± 2.2	312 ± 12
P6 (600 J/m)	32.4 ± 2.9	822 ± 3	849 ± 4	12.1 ± 1.9	311 ± 5
P8 (1200 J/m)	34.4 ± 2.4	893 ± 3	944 ± 3	9.9 ± 3.5	308 ± 6

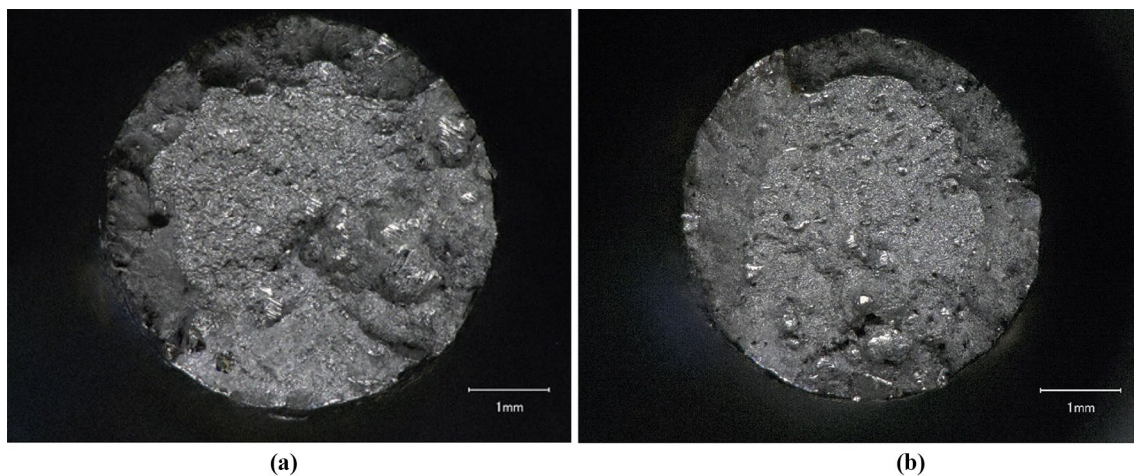


Fig. 6 Fracture surface of an as built EB-PBF manufactured Ti-5553 alloy using an E_L of **a** 150 J/m (P2) and **b** 600 J/m (P6)

Fig. 7 XRD pattern showing peaks for the α and β -phase of an as built EB-PBF manufactured Ti-5553 alloy using an E_L of 600 J/m (P6)

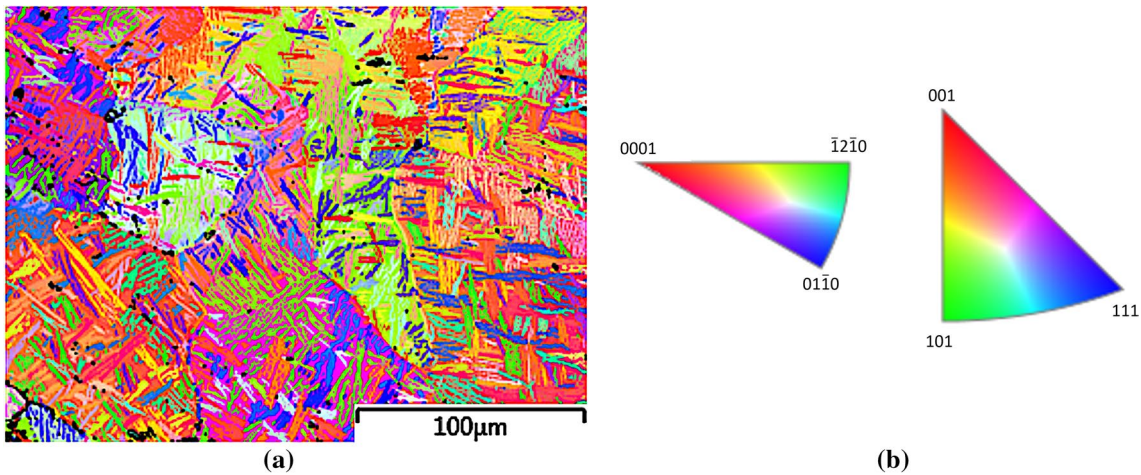
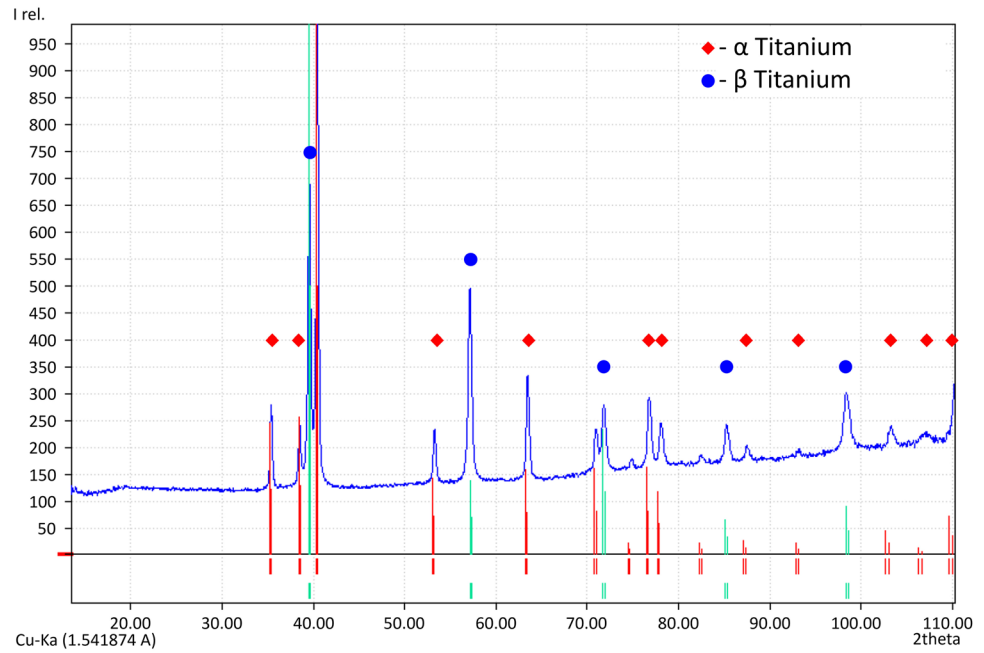


Fig. 8 **a** EBSD picture IPF Z and **b** direction map, of an as-built EB-PBF manufactured Ti-5553 alloy using an E_L of 600 J/m (P6)

Table 4 Mechanical properties of an as-built and heat-treated EB-PBF manufactured Ti-5553 alloy using an E_L of 600 J/m (P6)

Heat treatment	YS in MPa	UTS in MPa	El. at break in %
As built	822 ± 3	849 ± 4	12.1 ± 1.9
STA	1360 ± 14	1460 ± 21	4.2 ± 1.3
BASCA I	1429 ± 29	1504 ± 21	4.5 ± 0.4
BASCA II	888 ± 15	971 ± 13	22.1 ± 1.0

on the EB-PBF manufactured specimens. A summary of the mechanical properties after heat treatment is shown in Table 4. Heat treatments were performed for specimens of P2

($E_L = 150$ J/m), P6 ($E_L = 600$ J/m), and P9 ($E_L = 1800$ J/m), but due to their most promising combination of microstructure, mechanical properties, and density, only the results for P6 are presented and discussed in this work (Fig. 9).

Compared to the initial state, the use of the STA treatment step improves the mechanical strength and reduces elongation at break. Due to the high temperatures and long hold times during BASCA I and BASCA II heat treatments, there is a significant growth of precipitates, which strongly affects the mechanical properties. It is thus possible to set either a high strength, at an acceptable elongation at break, or an acceptable strength for a much larger elongation at break. Using the BASCA I heat treatment, an increase in strength of almost 80% can be achieved.

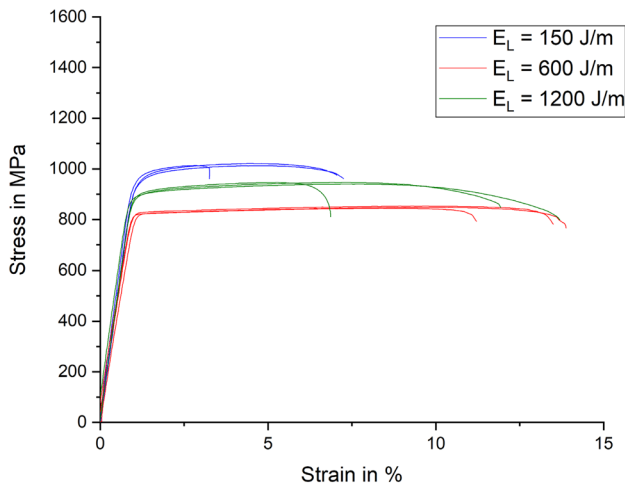


Fig. 9 Stress strain graph of as built EB-PBF manufactured Ti 5553 alloy using different E_L

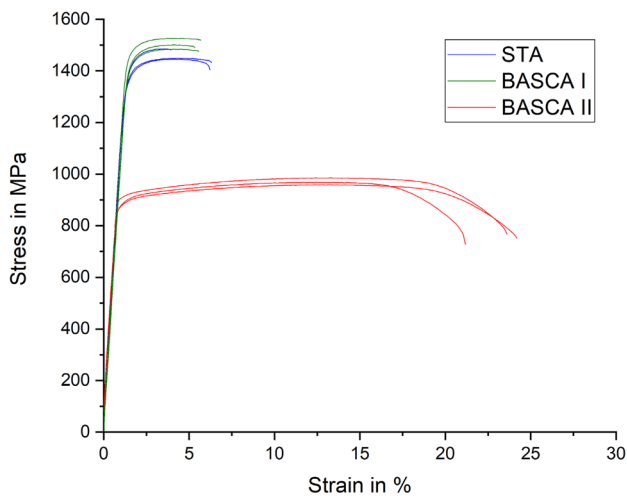


Fig. 10 Stress strain graph of heat-treated EB-PBF manufactured Ti-5553 alloy using an E_L of 600 J/m (P6)

Alternatively, if the BASCA II regime is used, the strength is only slightly increased, but the maximum elongation at break increases by 80%. The results of every tested specimen are summarized in Fig. 10.

The fracture surface of the STA specimen is presented in Fig. 11a. A constriction cannot be seen and is in line with the low elongation at break, see Fig. 11b. The fracture surface shows different fracture patterns throughout the fracture surface. In the area of crack nucleation, an intercrystalline fracture due to the smooth surface can be detected, see Fig. 11c. The fracture surface toward the middle of the specimen shows a more transcrystalline fracture. The characteristic honeycomb pattern is to be seen in Fig. 11d.

The fracture surface of the BASCA I heat-treated specimen is comparable to the fracture surface of the STA heat-treated specimens. A change in the morphology of the fracture surface can be seen in the heat-treated BASCA II specimens; see Fig. 12a. The side view of the fracture surface in Fig. 12b displays a strong constriction of the specimen under tensile force. The typical honeycomb pattern of transcrystalline fracture occurs over the full fracture surface, see Fig. 12c. In addition, Fig. 12d shows delamination as well as increased honeycomb size in the honeycomb pattern.

4 Discussion

4.1 Density

The inherent and, in the worst case, sharp-edged defects in additively manufactured components reduce the load-bearing cross-section of load-bearing parts and can act as crack nucleation sites. Therefore, the density and some specific characteristics, like the size and shape of pores and defects, are good indicators of the quality and the overall performance of manufactured parts [28]. Two different types of defects can be found in AM structures: (almost) spherical and/or irregularly shaped defects. The observed spherical defects are usually fairly small and filled with gas originating from either the gas atomization process or vaporization during the melting process (keyhole), see Fig. 13. The presence of large irregular-shaped defects, indicating either delamination, lack of fusion defects, or not fully melted powder, see Fig. 13, can lead to a critical failure of the part [26]. Unlike gas-filled defects (due to the gas trapped inside), irregularly shaped defects can mostly be eliminated using a hot isostatic pressure heat treatment [1].

The data obtained by the μ -CT show a strong correlation between E_L and the resulting density. The average density, shown in Table 2, is mainly influenced by the defect quantity and the corresponding size distribution. Since small defects are mainly irrelevant for the static mechanical behavior [27], the fraction-over-size ratio of defects is very important for the evaluation of the influence of defects. The results in Table 2 show that using a low E_L , specimens have the lowest absolute defect count, but the highest average defect size. This can be explained by the significantly smaller total number of defects, which means that the few large defects are likely to have a higher impact, compared to the case when there is a higher absolute pore count. Another explanation could be that due to the low E_L the electron beam does not supply enough energy. Consequently, the powder of the respective layer is not melted properly and good layer bonding cannot be achieved. Gong et al. [47] documented this phenomenon

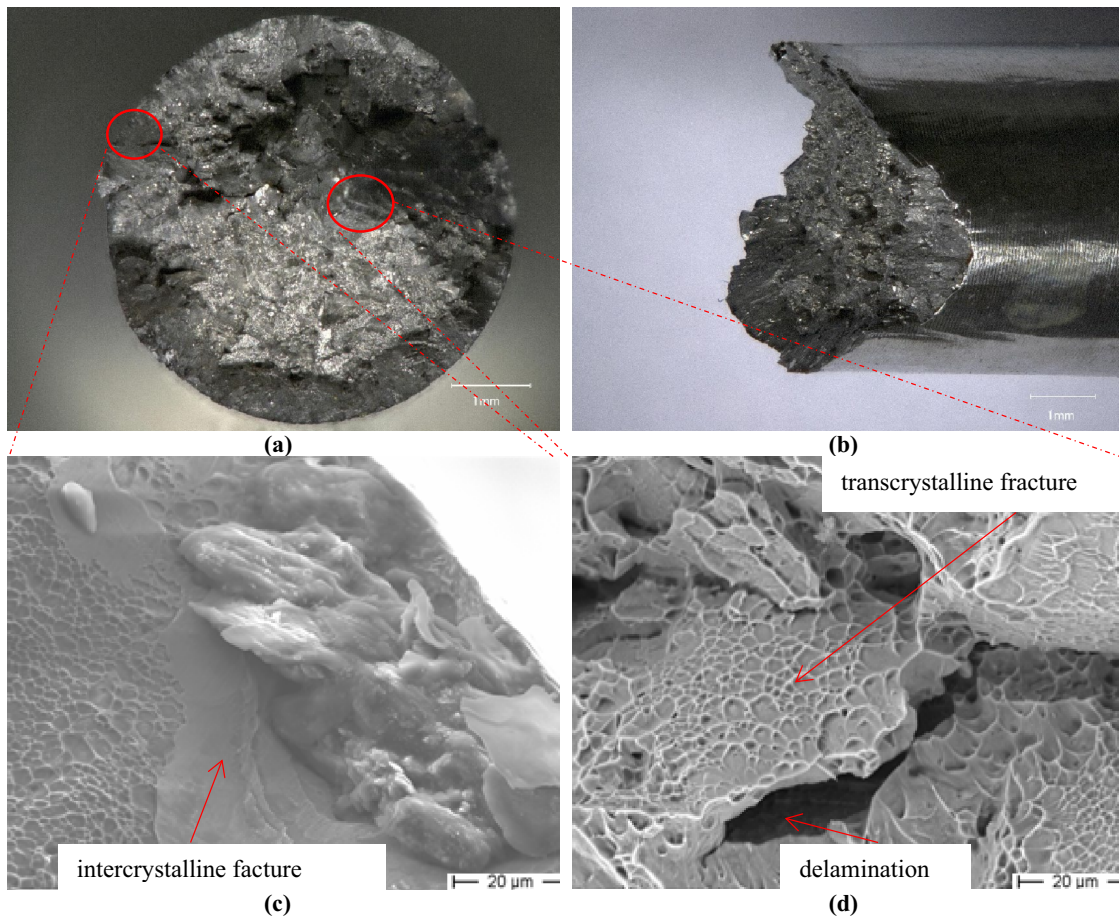


Fig. 11 **a** Fracture surface; **b**: side view of the fracture surface; **c** intercrystalline fracture area on the edge of the fracture surface; **d** transcrystalline fracture area toward the middle of the fracture surface

o of an STA heat-treated EB-PBF manufactured Ti-5553 alloy using an E_L of 600 J/m (P6)

for the L-PBF process where the defects increased with decreasing melting energy and became more irregularly shaped.

The fraction of 0–62 μm defects decreases, when using higher E_L , see Fig. 14a. For the small defect fraction (0–62 μm), a minimum of these fractions for specimens manufactured with an E_L of 400 and 600 J/m (see Table 1) can be seen (the P4 is more comparable to the P1–3 due to its low E_L). These small defects are mainly spherical and most likely gas-filled. These are formed mainly via keyhole mechanisms [48]. When comparing the fraction of defects from 62 to 102 μm , a low E_L leads to the smallest fraction ($\approx 35\%$). For larger E_L , the fraction rises to nearly 50%. The rest of the different defect ranges always show a comparable pattern. Specimens manufactured with low E_L have the highest fraction, which decreases toward higher E_L . As a result of the energy dependence of the defect size distribution, it can be concluded that the scanning speed and thus the energy introduced into the

powder have a strong influence on the defect size distribution. About 70% of the defects are smaller than 100 μm and 95% are smaller than 150 μm .

The $\mu\text{-CT}$ data were used to validate each defect regarding size and distribution, see Fig. 14b. The sphericity describes the shape of defects, where if it has a value of one the pore is perfectly round, typically these would be gas-filled defects. However, they compose only a minor part of all defects and as discussed above have only a minor impact on the static mechanical properties [27], but are likely to have an impact when performing cyclic fatigue testing [29]. The majority of the defects are irregular-shaped and have a size between 60 and 150 μm . Generally, defects reduce the load-bearing cross-section, and therefore, the material fails at lower stress levels. When determining the static mechanical properties, the defects play a minor role compared to the influence of the microstructure. However, this relationship only applies as long as a critical defect size and defect density are not

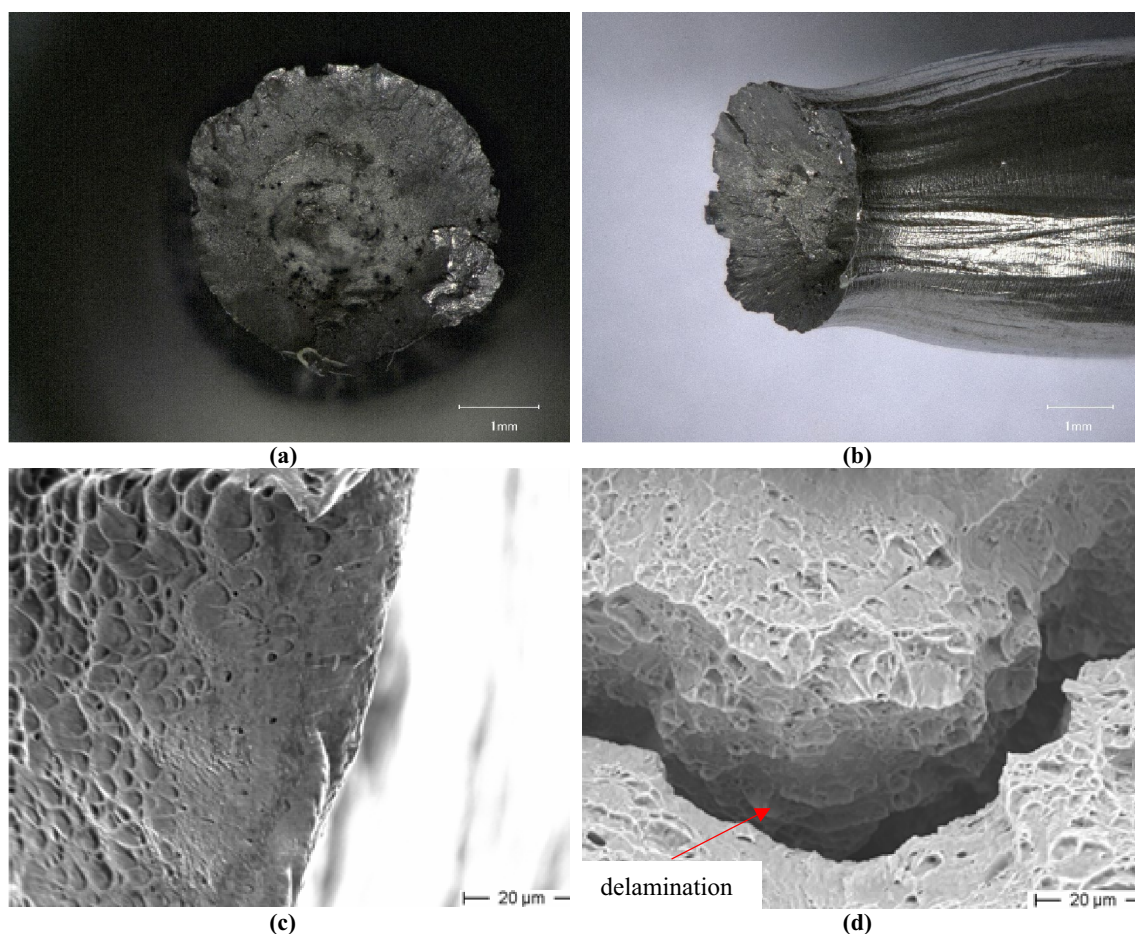


Fig. 12 **a** Fracture surface; **b** side view of the fracture surface; **c** transcrystalline fracture area on the edge of the fracture surface; **d** transcrystalline fracture area toward the middle of the fracture surface of

a BASCA II heat-treated EB-PBF manufactured Ti-5553 alloy using an E_L of 600 J/m (P6)

exceeded [49]. In this study, the specimens with the highest defects count (see Table 2) showed the lowest YS and UTS (see Table 3) of all tested specimens.

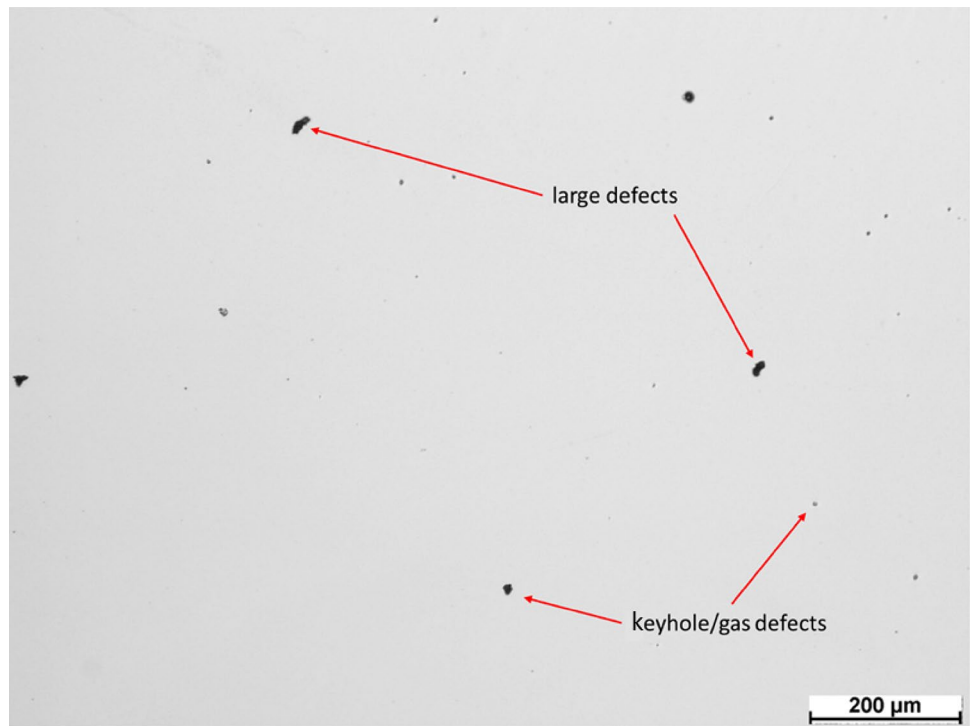
4.2 As-built mechanical properties and microstructure

The resulting as-built microstructure depends mainly on the energy introduced into the powder bed and thus on the temperature prevailing in the individual process steps. The energy that needs to be expended for the diffusion of aluminum is significantly lower for grain boundary diffusion compared to volume diffusion [50]. Aluminum is a strong α -stabilizer [12], and therefore, α_p is precipitated along the grain boundaries first, see Fig. 15a. The work of Schwab et al. [34] shows that the strong β -stabilizing alloying elements Mo, V, and Cr, due to their low solubility in α -titanium [51], diffuse from the precipitations into the β -matrix. Thus, the surrounding β -matrix is enriched with these elements [52] and inside the α precipitations, a large

supply of aluminum is present. During the production run of all used specimens, the temperature was above 500 °C, see Fig. 3, and a slow cooling occurred. Therefore, it can be assumed that no ω -phase is present in the microstructure [3]. Due to the high temperature inside the building chamber, α precipitations can grow into large lamellar needles as the EB-PBF process progresses. Compared to α_p precipitations, α_s precipitations require lower temperatures to form and grow nuclei. With every additional added powder layer in the production run, the energy conducted downwards from the top layer decreases, and the temperature decreases slowly, see Fig. 3

If the local temperature drops permanently below roughly 600 °C, α_s start to precipitate [12], see Fig. 15a. These α_s precipitations grow from different nucleation sites (Widmanschstätten) in every direction, and after long isothermal holding times, these start to rearrange into small triangles [46]. Jones et al. [46] suggest that each needle is on one {110} β -habit plane with an angle between them of 60°, see Fig. 15b. Due to the lower energy supply during the α_s

Fig. 13 Typical defects of an additively manufactured EB-PBF Ti-5553 alloy using an E_L of 600 J/m (P6), optical microscope



precipitation, the needles stay very fine. Using EBSD, see Fig. 18, a combined α precipitation fraction of 43% was measured. In Table 3, the influence on microstructure and consequential mechanical properties can be seen due to the variation of beam parameters and hence E_L . One main discovery of this work is that by decreasing the scanning speed and increasing the E_L into the powder bed, the α_p fraction increases. Due to this higher energy density and, therefore, longer time at higher temperatures, the precipitation fraction of α_p is increased. Furthermore, these can grow further

during the subsequent building process. Consequently, the fine α_s fraction decreases, see Figs. 15, 16, and 17. This study has shown that above $E_L = 400$ J/m, the α_p fraction reaches a constant value of 35%. Since all specimens were manufactured in the same production run, the manufacturing conditions were similar except for the beam parameters used to melt the specimens. The results suggest that at E_L above 400 J/m, the temperature control due to self-cooling is constant for each specimen. Thus, no additional α_p can be precipitated and a limit value of 35% for the α_p

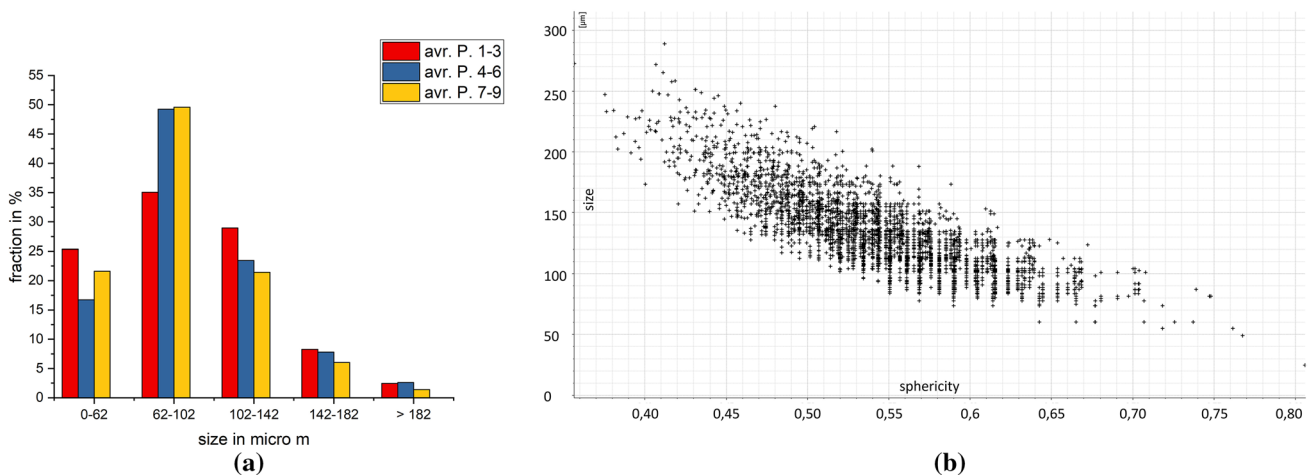


Fig. 14 **a** Dependence of the defect size distribution of EB-PBF manufactured Ti-5553 using all investigated E_L from 75 to 1800 J/m, and **b** resulting defect size dependence on sphericity of an EB-PBF manufactured Ti-5553 using an E_L of 150 J/m (P2)

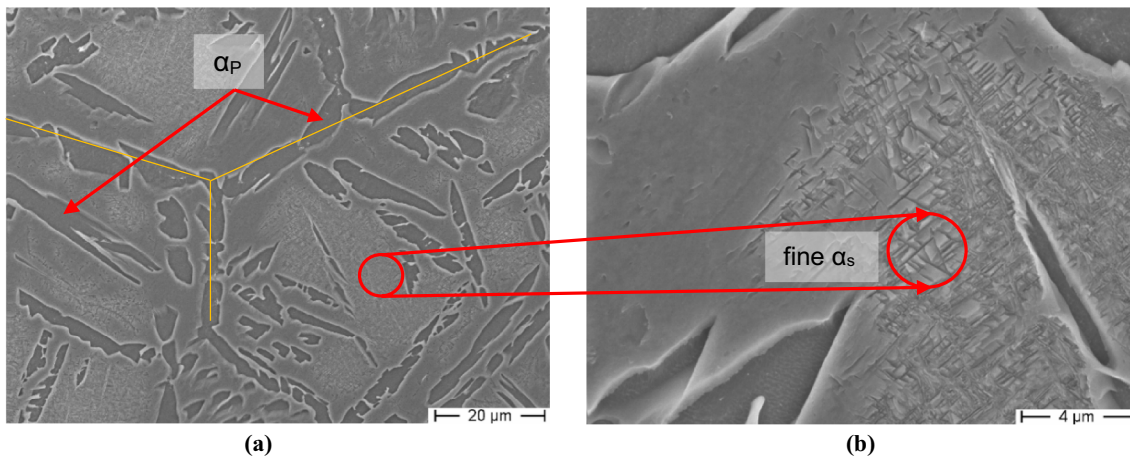


Fig. 15 As-built microstructure consisting of a β -matrix, and coarse α_p and fine α_s precipitations of an EB-PBF manufactured Ti-5553 alloy using an E_L of 150 J/m (P2), SEM, (b) is a higher magnification of (a)

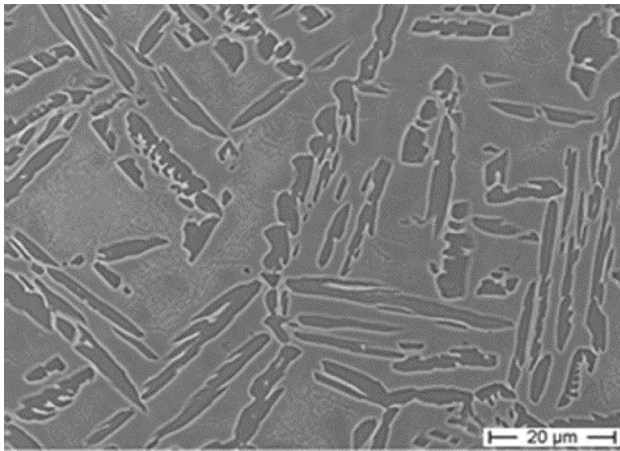


Fig. 16 As-built microstructure consisting of a β -matrix, and coarse α_p and fine α_s precipitations of an EB-PBF manufactured Ti-5553 alloy using an E_L of 400 J/m (P5), SEM

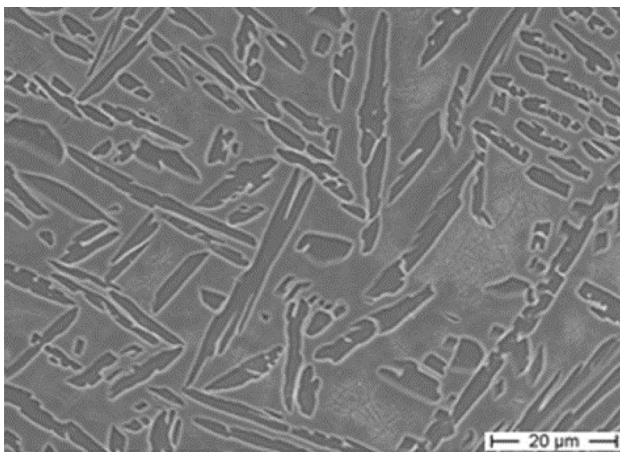


Fig. 17 As-built microstructure consisting of a β -matrix, and coarse α_p and fine α_s precipitations of an EB-PBF manufactured Ti-5553 alloy using an E_L of 1200 J/m (P8), SEM

fraction can be achieved. By correlating the microstructure with the mechanical properties, the results indicate that the ratio of the small, acicular α precipitations, large lamellar precipitations, and β -matrix have a strong impact on the static mechanical properties of the specimens [9]. Fine α_s precipitations increase, compared to larger precipitations, the number of interfaces between them and the surrounding β -matrix. These interfaces act as dislocation barriers. Therefore, the strength of the material rises with an increasing fraction of acicular α_s precipitations. Li et al. [53] have shown that for high-strength Ti-alloys, α_p has a direct influence on the achieved elongation at break and accompanying ductility. A larger α_p fraction leads, due to slipping and shearing processes in large precipitations, to significant enhancements of the elongations at break [9], see Table 3. Consequently, due to the lower fraction of α_s precipitations for specimens melted with increased E_L , the ultimate tensile strength is reduced (Figs. 9, 18). The decreased mechanical properties of specimens manufactured with P6 (600 J/m) can be explained by the substantial number of large defects, see Fig. 9a, and decreased average density, see Table 2. The fracture surfaces of the specimens manufactured with different melting parameters show, depending on their respective microstructure, very different patterns, and appearances. As already mentioned, the specimen with a lower α_p fraction exhibits higher mechanical strength but a lower elongation at break. This can be seen when comparing Fig. 7a, b. The specimens with the lower elongation at break (P2) show less constriction and overall deformation than the specimens with the higher elongation at break (P6).

A comparison between the microstructures and mechanical properties of manufactured parts using EB-PBF and L-PBF is very difficult due to the different process parameters. The temperatures and cooling rates prevailing in the processes and thus the different property-determining

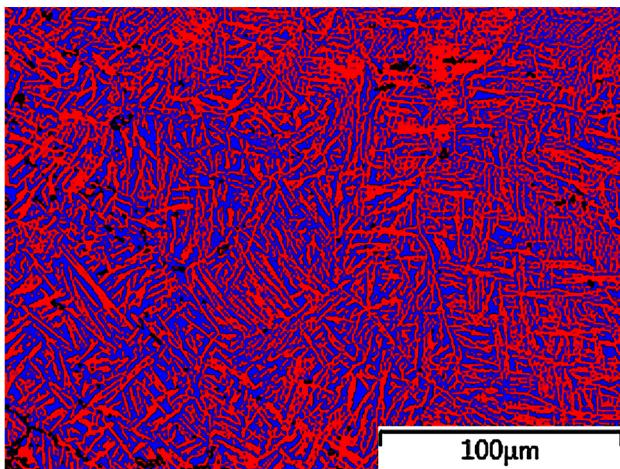


Fig. 18 EBSD phase fraction measurement of an EB-PBF manufactured Ti-5553 alloy using an E_L of 600 J/m (P6), blue = β -Ti, and red = α -Ti

microstructure development are very significantly influenced by the selected process parameters. The main difference is the high processing temperature during the EB-PBF process and the associated introduction of α precipitations. Schwab et al. [33] manufactured Ti-5553 using L-PBF and was able to achieve a single-phase (β -phase) microstructure. When they used an additional building platform heating α precipitations were observed due to the higher temperature during the L-PBF process [34]. Liu and Qiu [35, 36] showed in their work that the microstructure results, due to the rapid cooling of L-PBF manufactured Ti-1023 samples, in a β -matrix with ω precipitations. When a higher energy density was used, α was additionally found next to the ω precipitations.

4.3 Heat treatment

4.3.1 Solution treated and aged-STA

By solution treating the specimens underneath T_{β} , the total energy supplied to the specimens is too low to completely dissolve the original microstructure. Under these conditions, there is a coarsening of the as-built microstructure. In addition, α_p is further precipitated, see Fig. 19a. When quenching to room-temperature diffusion and thus growing processes are almost completely suppressed. The microstructure indicates that very fine α_s are precipitated for a short period during the quenching process. At the aging temperature of 500 °C, α_s can further precipitate, but the short dwell time (60 min) does not result in nominal grain growth of these precipitated phase fraction, see Fig. 19a. As a result of the small size and homogenous distribution of α_s in the β -matrix, a lot of dislocation barriers exist and, therefore, the mechanical strength improves, see Table 4. The fracture surface, see Fig. 11, appears, due to the almost identical elongation at break, comparable with the as-built fracture surfaces, see Fig. 6b. Due to the small α_p fraction and the very fine α_s precipitations, the STA heat-treated specimens fail with a mixed fracture pattern and with no detectable constriction. The area in Fig. 11c shows residues of powder particles, which were not fully melted, thus creating a weak spot and forming the crack nucleation site. Delaminations, see Fig. 11d, often originate from lack of fusion defects and reduce the mechanical properties. The measured static mechanical properties ($YS = 1360$ MPa; $UTS = 1460$ MPa) can be compared to the results of the conventionally produced and forged specimens from other research groups [10]. Sadeghpour et al. [9] have shown that higher temperatures and longer holding times for the solution as well as the aging step lead to decreased

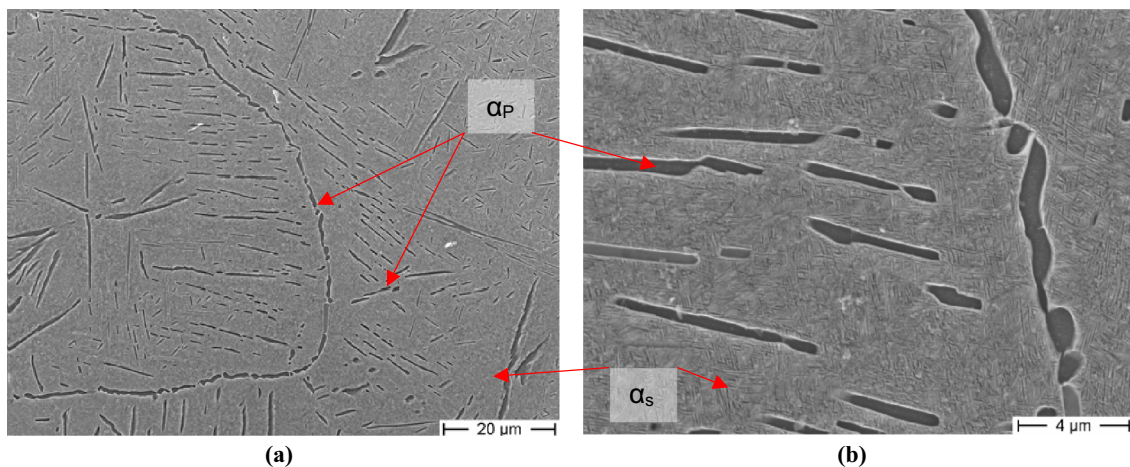


Fig. 19 STA microstructure consisting of a β -matrix, and coarse α_p and fine α_s precipitations of heat-treated EB-PBF manufactured Ti-5553 alloy using an E_L of 600 J/m (P6), SEM; **b** is a higher magnification of **a**)

strength (YS = 1100 MPa; UTS = 1150 MPa) and increased elongation at break ($\epsilon = 10\%$).

4.3.2 Beta annealed, slow cooled, and aged-BASCA I

This solution treatment is carried out at 870 °C and hence above T_β . The available total energy during the solution step is sufficient to enable the dissolution of the original microstructure. During quenching to room temperature very fine α_p is precipitated, as discussed above, along the grain boundary, see Fig. 20a. When the temperature drops below 600 °C, α_s precipitate inside the β -grains. In a comparable manner to behavior during the aging step of the STA heat treatment, the precipitated phase fractions cannot grow further at the aging temperature of 570 °C. However, the temperature in combination with the long holding times is sufficient to arrange the needles into a triangular shape (compare to Sect. 3.2), see Fig. 20b. The precipitation size achieved using this heat treatment is very small. As a result, the YS could be increased by 70–1429 MPa compared to the STA treated specimens, see Table 4. Compared with the work of other research groups that have studied conventionally manufactured Ti-5553 alloys, the mechanical strength is improved in this work. Musi et al. [54] use slightly different temperatures for the BASCA heat treatment, resulting in a different phase fraction and distribution of β -matrix and precipitations ($\alpha_p + \alpha_s$). Hence the YS (965 MPa), as well as the UTS (1103 MPa), is decreased, but the elongation at break is enhanced (6%) compared to this work.

4.3.3 Beta annealed, slow cooled, and aged-BASCA II

The increased solution treatment temperature (890 °C) and long holding times (90 min) ensure complete dissolution of

the as-built microstructure during the annealing step. The controlled cooling (2 K/min) in the oven toward the aging temperature of 600 °C causes α_p precipitation. In contrast to the STA and BASCA I heat treatments, the α_s precipitations are not only formed in the BASCA II heat treatment but also continue to grow under the process conditions due to the slightly elevated temperatures in the aging step. The long holding time results in a microstructure of large lamellar precipitations, Fig. 21a, embedded in a coarse β -matrix, Fig. 21b. Other research groups show that next to the amount of β -phase in the matrix, the fractions of lamellar and acicular α precipitations are responsible for enhancing ductility [9, 10]. Large α_p and α_s precipitations can be deformed by slipping and shearing mechanisms [9]. Huang et al. [55] have shown that α precipitations with 5–10 μm can also deform via the twinning mechanism. Due to the larger fraction of lamellar α precipitations, a smaller number of dislocations can accumulate compared to cases for the STA or BASCA I heat treatments. Consequently, the comparative mechanical strength increases only slightly, see Table 4. Due to the bcc structure of the β -phase and the larger number of available deformation mechanisms, the elongation at break increases, and the deformability is enhanced [12]. This is also evident from the respective fracture surface. Comparing the surfaces of the STA specimen, Fig. 11, and the BASCA II specimen, Fig. 12, a significant difference in appearance can be seen. A severe constriction can be noticed, which is due to the much more ductile failure compared to the heat-treated STA or BASCA I specimens. Figure 12c, d shows a similar fracture pattern over the entire fracture surface of the specimen.

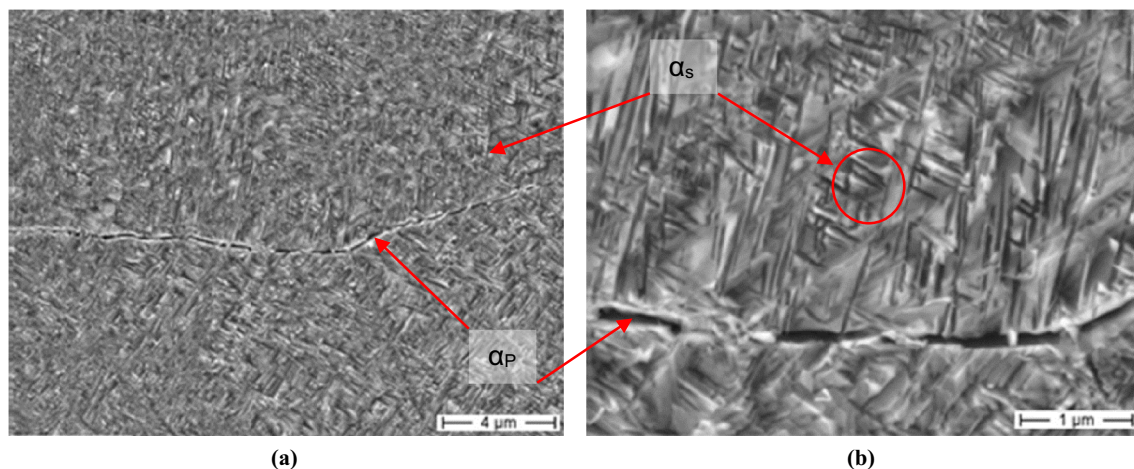


Fig. 20 BASCA I microstructure consisting of a β -matrix and very fine α_p (just alongside the grain boundaries) as well as very fine α_s precipitations in the heat-treated EB-PBF manufactured Ti-5553 alloy

using an E_L of 600 J/m (P6), SEM. **b** Higher magnification of the microstructure of (a)

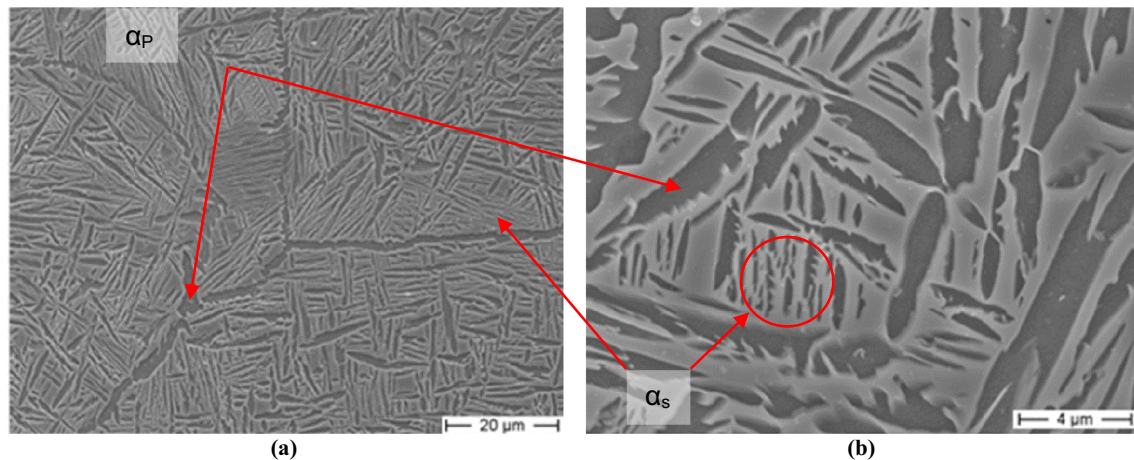


Fig. 21 BASCA II microstructure consisting of a β -matrix and coarse α_p as well as α_s precipitations of heat-treated EB-PBF manufactured Ti-5553 alloy using an E_L of 600 J/m (P6), SEM. The right figure shows a magnification of the left figure

5 Conclusions

The present work has demonstrated the potential for the manufacture of very high density ($\rho > 99.6\%$) Ti-5553 parts using the EB-PBF process. The μ -CT data revealed that most of the defects (roughly 95%) are smaller than 150 μm and irregularly shaped. The achieved relative density is comparable with those of other AM processes, like L-PBF.

By varying process parameters, nine different specimens were manufactured. The microstructure of all specimens showed coarse β -grains, large α_p precipitations (precipitating below T_β but above 600 $^\circ\text{C}$), and fine α_s precipitations (precipitating below 600 $^\circ\text{C}$) acting as the strengthening phase. The presence of the ω -phase can be excluded due to the high temperatures throughout the EB-PBF process as well as the slow cooling rate after the production run. The α_p -phase reached an as-built volume fraction of up to 35%, and therefore, it can strongly influence the mechanical behavior. When correlating the mechanical strength with the defect structure and microstructure for the as-built specimens, it was seen that a higher α_p fraction resulted in increased elongations at break due to more slip and shear processes. The very fine α_s precipitations act as dislocation barriers, and therefore, a high α_s fraction leads to high mechanical strength and decreased elongations at break. In conclusion, it can be suggested that for highly dense specimens, the tailored microstructure, especially the ratio between α_p and α_s , has a major influence on the static mechanical properties. However, the relative density and the respective defect structure must be considered. A high number of (very large) defects will cause there to be a multitude of crack nucleation sites (especially regarding fatigue properties) and these can therefore reduce the mechanical strength. In general, a high relative density and a low number of defects should be desired if a good

mechanical strength of additively manufactured parts is sought after.

By applying different heat treatments, the mechanical properties can be tailored for different applications. Utilizing the STA and BASCA I heat-treatment cycles allows Ti-5553 specimens with high mechanical strength and adequate elongation at break to be produced. The very fine and numerous α_s precipitations are responsible for the excellent mechanical strength. The BASCA II heat treatment favors the formation of microstructure components, which enable a high ductility of the Ti-5553 specimens. The microstructure, with its large lamellar α precipitations as well as the large β -phase matrix, provides a high elongation at break and a, compared to the as-built samples, slightly improved mechanical strength. The results of this work indicate that the EB-PBF-manufactured Ti-5553 alloy can be used for a wide range of applications. By varying the heat-treatment cycle, the microstructure and, therefore, the static mechanical properties can be adjusted to allow very high mechanical strengths of UTS (1500 MPa) and sufficient elongation at break (4%) or excellent elongations at break (22%) with sufficient UTS (920 MPa). To minimize the occurrence of lack of fusion defects, post-heat treatment with hot isostatic pressing could be considered. This can lead to a further improvement of the mechanical properties.

Acknowledgements The authors would like to thank the BMBF (Bundesministerium für Bildung und Forschung) for the financial support within the “AGENT-3D_Basis” project (Funding Code 03ZZ0204B).

Authors' contributions Conceptualization: AM; methodology: JH and AM; data curation: JH and AM; formal analysis and investigation: JH; validation: JH and AM; writing—original draft preparation: JH; writing—review and editing: JH, AM, and CL; funding acquisition: CL; resources: AM and CL; supervision: AM; project administration: AM and CL.

Funding Open Access funding enabled and organized by Projekt DEAL.

Declarations

Conflict of interest On behalf of all authors, the corresponding author states that there is no conflict of interest.

Open Access This article is licensed under a Creative Commons Attribution 4.0 International License, which permits use, sharing, adaptation, distribution and reproduction in any medium or format, as long as you give appropriate credit to the original author(s) and the source, provide a link to the Creative Commons licence, and indicate if changes were made. The images or other third party material in this article are included in the article's Creative Commons licence, unless indicated otherwise in a credit line to the material. If material is not included in the article's Creative Commons licence and your intended use is not permitted by statutory regulation or exceeds the permitted use, you will need to obtain permission directly from the copyright holder. To view a copy of this licence, visit <http://creativecommons.org/licenses/by/4.0/>.

References

1. DebRoy T, Wei HL, Zuback JS, Mukherjee T, Elmer JW, Milewski JO, Beese AM, Wilson-Heid A, De A, Zhang W (2018) Additive manufacturing of metallic components—process, structure and properties. *Prog Mater Sci* 92:112–224. <https://doi.org/10.1016/j.pmatsci.2017.10.001>
2. Gerday AF (2009) Mechanical behavior of Ti-5553 alloy modeling of representative cells, University of Liège
3. Zheng Y, Williams REA, Sosa JM, Wang Y, Banerjee R, Fraser HL (2016) The role of the ω phase on the non-classical precipitation of the α phase in metastable β -titanium alloys. *Scr Mater* 111:81–84. <https://doi.org/10.1016/j.scriptamat.2015.08.019>
4. Furuhashi T, Ogawa T, Maki T (1995) Atomic structure of interphase boundary of an α precipitate plate in a β Ti[*s*bn]Cr alloy. *Philos Mag Lett* 72:175–183. <https://doi.org/10.1080/09500839508242449>
5. Furuhashi T, Howe JM, Aaronson HI (1991) Interphase boundary structures of intragranular proeutectoid α plates in a hypoeutectoid TiCr alloy. *Acta Metall Mater* 39:2873–2886
6. Menon ESK, Aaronson HI (1986) Interfacial structure of Widmanstätten plates in a TiCr alloy. *Acta Metall* 34:1975–1981. [https://doi.org/10.1016/0001-6160\(86\)90256-7](https://doi.org/10.1016/0001-6160(86)90256-7)
7. Shi R, Ma N, Wang Y (2012) Predicting equilibrium shape of precipitates as function of coherency state. *Acta Mater* 60:4172–4184. <https://doi.org/10.1016/j.actamat.2012.04.019>
8. Dehghan-Manshadi A, Dippenaar RJ (2011) Development of α -phase morphologies during low temperature isothermal heat treatment of a Ti–5Al–5Mo–5V–3Cr alloy. *Mater Sci Eng A* 528:1833–1839. <https://doi.org/10.1016/j.msea.2010.09.061>
9. Sadeghpour S, Abbasi SM, Morakabati M, Bruschi S (2017) Correlation between alpha phase morphology and tensile properties of a new beta titanium alloy. *Mater Des* 121:24–35. <https://doi.org/10.1016/j.matdes.2017.02.043>
10. Panza-Giosa R (2008) Mechanical properties of heat treated Ti-5Al-5V-5Mo-3Cr—an attempt to define critical properties of various microstructural features. Las Vegas, p 35
11. Nyakana SL, Fanning JC, Boyer RR (2005) Quick reference guide for β titanium alloys in the 00s. *J Mater Eng Perform* 14:799–811. <https://doi.org/10.1361/105994905X75646>
12. Leyens C, Peters M (eds) (2003) Titanium and titanium alloys: fundamentals and applications. Wiley-VCH Verlag GmbH & Co. KGaA, Weinheim. <https://doi.org/10.1002/3527602119>
13. Boyer R, Briggs R, Veeck S, Lee D (2004) The castability of Ti-5553 alloy. *Adv Mater* 3
14. Baili M, Wagner V, Dessein G, Sallaberry J, Lallemand D (2011) An experimental investigation of hot machining with induction to improve Ti-5553 machinability. *Appl Mech Mater* 62:67–76. <https://doi.org/10.4028/www.scientific.net/AMM.62.67>
15. Walton D, Moztarzadeh H (2017) Design and development of an additive manufactured component by topology optimisation. *Proc CIRP* 60:205–210. <https://doi.org/10.1016/j.procir.2017.03.027>
16. Bourell D, Kruth JP, Leu M, Levy G, Rosen D, Beese AM, Clare A (2017) Materials for additive manufacturing. *CIRP Ann* 66:659–681. <https://doi.org/10.1016/j.cirp.2017.05.009>
17. Seabra M, Azevedo J, Araújo A, Reis L, Pinto E, Alves N, Santos R, Pedro Mortágua J (2016) Selective laser melting (SLM) and topology optimization for lighter aerospace components. *Proc Struct Integr* 1:289–296. <https://doi.org/10.1016/j.prostr.2016.02.039>
18. Emmelmann C, Petersen M, Kranz J, Wycisk E (2011) Bionic lightweight design by laser additive manufacturing (LAM) for aircraft industry. In: Ambs P, Curticepan D, Emmelmann C, Knapp W, Kuznicki ZT, Meyrueis PP (eds) Strasbourg, France, p 80650L. <https://doi.org/10.1117/12.898525>
19. Willner R, Lender S, Ihl A, Wilsnack C, Gruber S, Brandão A, Pambaguian L, Riede M, López E, Brueckner F, Leyens C (2020) Potential and challenges of additive manufacturing for topology optimized spacecraft structures. *J Laser Appl* 32:032012. <https://doi.org/10.2351/7.0000111>
20. Khajavi SH, Partanen J, Holmström J (2014) Additive manufacturing in the spare parts supply chain. *Comput Ind* 65:50–63. <https://doi.org/10.1016/j.compind.2013.07.008>
21. Herzog D, Seyda V, Wycisk E, Emmelmann C (2016) Additive manufacturing of metals. *Acta Mater* 117:371–392. <https://doi.org/10.1016/j.actamat.2016.07.019>
22. Uriondo A, Esperon-Miguez M, Perinpanayagam S (2015) The present and future of additive manufacturing in the aerospace sector: a review of important aspects. *Proc Inst Mech Eng Part G J Aerosp Eng* 229:2132–2147. <https://doi.org/10.1177/0954410014568797>
23. Narayana PL, Li C-L, Kim S-W, Kim S-E, Marquardt A, Leyens C, Reddy NS, Yeom J-T, Hong J-K (2019) High strength and ductility of electron beam melted β stabilized γ -TiAl alloy at 800°C. *Mater Sci Eng A* 756:41–45. <https://doi.org/10.1016/j.msea.2019.03.114>
24. Biamino S, Penna A, Ackelid U, Sabbadini S, Tassa O, Fino P, Pavese M, Gennaro P, Badini C (2011) Electron beam melting of Ti–48Al–2Cr–2Nb alloy: microstructure and mechanical properties investigation. *Intermetallics* 19:776–781. <https://doi.org/10.1016/j.intermet.2010.11.017>
25. Masuo H, Tanaka Y, Morokoshi S, Yagura H, Uchida T, Yamamoto Y, Murakami Y (2018) Influence of defects, surface roughness and HIP on the fatigue strength of Ti-6Al-4V manufactured by additive manufacturing. *Int J Fatigue* 117:163–179. <https://doi.org/10.1016/j.ijfatigue.2018.07.020>
26. Carlton HD, Haboub A, Gallegos GF, Parkinson DY, MacDowell AA (2016) Damage evolution and failure mechanisms in additively manufactured stainless steel. *Mater Sci Eng A* 651:406–414. <https://doi.org/10.1016/j.msea.2015.10.073>
27. Liu F, He C, Chen Y, Zhang H, Wang Q, Liu Y (2020) Effects of defects on tensile and fatigue behaviors of selective laser melted titanium alloy in very high cycle regime. *Int J Fatigue* 140:105795. <https://doi.org/10.1016/j.ijfatigue.2020.105795>

28. Fatemi A, Molaei R, Simsiriwong J, Sanaei N, Pegues J, Torries B, Phan N, Shamsaei N (2019) Fatigue behaviour of additive manufactured materials: an overview of some recent experimental studies on Ti-6Al-4V considering various processing and loading direction effects. *Fatigue Fract Eng Mater Struct* 42:991–1009. <https://doi.org/10.1111/ffe.13000>
29. Yadollahi A, Shamsaei N (2017) Additive manufacturing of fatigue resistant materials: challenges and opportunities. *Int J Fatigue* 98:14–31. <https://doi.org/10.1016/j.ijfatigue.2017.01.001>
30. Hicks C, Konkova T, Blackwell P (2020) Influence of laser power and powder feed rate on the microstructure evolution of laser metal deposited Ti-5553 on forged substrates. *Mater Charact* 170:110675. <https://doi.org/10.1016/j.matchar.2020.110675>
31. Ansari M, Martinez-Marchese A, Huang Y, Toyserkani E (2020) A mathematical model of laser directed energy deposition for process mapping and geometry prediction of Ti-5553 single-tracks. *Materialia* 12:100710. <https://doi.org/10.1016/j.mtla.2020.100710>
32. Zopp C, Blümer S, Schubert F, Kroll L (2017) Processing of a metastable titanium alloy (Ti-5553) by selective laser melting. *Ain Shams Eng J* 8:475–479. <https://doi.org/10.1016/j.asej.2016.11.004>
33. Schwab H, Palm F, Kühn U, Eckert J (2016) Microstructure and mechanical properties of the near-beta titanium alloy Ti-5553 processed by selective laser melting. *Mater Des* 105:75–80. <https://doi.org/10.1016/j.matdes.2016.04.103>
34. Schwab H, Bönisch M, Giebeler L, Gustmann T, Eckert J, Kühn U (2017) Processing of Ti-5553 with improved mechanical properties via an in-situ heat treatment combining selective laser melting and substrate plate heating. *Mater Des* 130:83–89. <https://doi.org/10.1016/j.matdes.2017.05.010>
35. Qiu C, Liu Q (2019) Multi-scale microstructural development and mechanical properties of a selectively laser melted beta titanium alloy. *Addit Manuf* 30:100893. <https://doi.org/10.1016/j.addma.2019.100893>
36. Liu Q, Qiu C (2020) Variant selection of α precipitation in a beta titanium alloy during selective laser melting and its influence on mechanical properties. *Mater Sci Eng A* 784:139336. <https://doi.org/10.1016/j.msea.2020.139336>
37. Azizi H, Zurob H, Bose B, Reza Ghiaasiaan S, Wang X, Coulson S, Duz V, Phillion AB (2018) Additive manufacturing of a novel Ti-Al-V-Fe alloy using selective laser melting. *Addit Manuf* 21:529–535. <https://doi.org/10.1016/j.addma.2018.04.006>
38. Colombo-Pulgarín JC, Biffi CA, Vedani M, Celentano D, Sánchez-Egea A, Boccardo AD, Ponthot J-P (2021) Beta titanium alloys processed by laser powder bed fusion: a review. *J Mater Eng Perform*. <https://doi.org/10.1007/s11665-021-05800-6>
39. Sames WJ, List FA, Pannala S, Dehoff RR, Babu SS (2016) The metallurgy and processing science of metal additive manufacturing. *Int Mater Rev* 61:315–360. <https://doi.org/10.1080/09506608.2015.1116649>
40. Lawley A (1981) Atomization of specialty alloy powders. *JOM* 33:13–18. <https://doi.org/10.1007/BF03354395>
41. Seidel A, Saha S, Maiwald T, Moritz J, Polenz S, Marquardt A, Kaspar J, Finaske T, Lopez E, Brueckner F, Leyens C (2019) Intrinsic heat treatment within additive manufacturing of gamma titanium aluminide space hardware. *JOM* 71:1513–1519. <https://doi.org/10.1007/s11837-019-03382-2>
42. DIN Deutsches Institut für Normung e. V. (2017) DIN EN ISO 6892-1, Beuth, Berlin
43. DIN Deutsches Institut für Normung e. V. (2016) DIN EN ISO 6057-1, Beuth, Berlin
44. Ghosh A, Sivaprasad S, Bhattacharjee A, Kar SK (2013) Microstructure–fracture toughness correlation in an aircraft structural component alloy Ti-5Al-5V-5Mo-3Cr. *Mater Sci Eng A* 568:61–67. <https://doi.org/10.1016/j.msea.2013.01.017>
45. Chretien A, Freundlich W, Bichara M (1954) Etude du systeme titane-hydrogene; preparation d'un hydrure de titane, TiH₂. *Comptes Rendus* 1423–1424
46. Jones NG, Dashwood RJ, Jackson M, Dye D (2009) β Phase decomposition in Ti-5Al-5Mo-5V-3Cr. *Acta Mater* 57:3830–3839. <https://doi.org/10.1016/j.actamat.2009.04.031>
47. Gong H, Rafi K, Gu H, Janaki Ram GD, Starr T, Stucker B (2015) Influence of defects on mechanical properties of Ti-6Al-4V components produced by selective laser melting and electron beam melting. *Mater Des* 86:545–554. <https://doi.org/10.1016/j.matdes.2015.07.147>
48. King WE, Barth HD, Castillo VM, Gallegos GF, Gibbs JW, Hahn DE, Kamath C, Rubenchik AM (2014) Observation of keyhole-mode laser melting in laser powder-bed fusion additive manufacturing. *J Mater Process Technol* 214:2915–2925. <https://doi.org/10.1016/j.jmatprotec.2014.06.005>
49. Hendl J, Daubner S, Marquardt A, Stepien L, Lopez E, Brückner F, Leyens C (2021) In situ CT tensile testing of an additively manufactured and heat-treated metastable β -titanium alloy (Ti-5Al-5Mo-5V-3Cr). *Appl Sci* 11:9875. <https://doi.org/10.3390/app11219875>
50. Callister WD (2001) Fundamentals of materials science and engineering: an interactive etext. Wiley, New York
51. Lütjering G, Williams JC (2007) Titanium, 2. Springer, Heidelberg
52. Takase A, Ishimoto T, Suganuma R, Nakano T (2021) Surface residual stress and phase stability in unstable β -type Ti-15Mo-5Zr-3Al alloy manufactured by laser and electron beam powder bed fusion technologies. *Addit Manuf* 47:102257. <https://doi.org/10.1016/j.addma.2021.102257>
53. Li C-L, Mi X-J, Ye W-J, Hui S-X, Yu Y, Wang W-Q (2013) Effect of solution temperature on microstructures and tensile properties of high strength Ti-6Cr-5Mo-5V-4Al alloy. *Mater Sci Eng A* 578:103–109. <https://doi.org/10.1016/j.msea.2013.04.063>
54. Musi D (2005) An update on properties and applications for Ti-5Al-5Mo-5V-3Cr. In: Titan. 2005 Conf. Proc., Scottsdale, Arizona
55. Huang C, Zhao Y, Xin S, Zhou W, Li Q, Zeng W (2017) Effect of microstructure on tensile properties of Ti-5Al-5Mo-5V-3Cr-1Zr alloy. *J Alloys Compd* 693:582–591. <https://doi.org/10.1016/j.jallcom.2016.09.233>

Publisher's Note Springer Nature remains neutral with regard to jurisdictional claims in published maps and institutional affiliations.